Electrochemical performance and degradation behaviour of Ni–YSZ anode-supported SOFC operated with pre-processed biogas

Electrochimica Acta 568 (2026) 148838

Contents lists available at ScienceDirect

Electrochimica Acta

journal homepage: www.journals.elsevier.com/electrochimica-acta

Electrochemical performance and degradation behaviour of Ni–YSZ anode-supported SOFC operated with pre-processed biogas

Lucia Pera [a,b], Cédric Frantz [b], Hangyu Yu [b,*], Marta Gandiglio [a], Paolo Marocco [a], Massimo Santarelli [a], Jan Van Herle [b]

[a] Department of Energy, Politecnico di Torino, Corso Duca degli Abruzzi 24, 10129 Torino, Italy
[b] Group of Energy Materials, Swiss Federal Institute of Technology in Lausanne (EPFL), Rue de l'Industrie 17, Sion, 1950 Valais, Switzerland

ARTICLE INFO

Keywords:
Anode-supported cell
Biogas
SOFC degradation
Electrochemical impedance spectroscopy
ECM fitting

ABSTRACT

Solid Oxide Fuel Cells (SOFCs) offer high efficiency and fuel flexibility, yet their long-term stability under biogas-derived fuels remains insufficiently understood. This work investigates the electrochemical behaviour and degradation mechanisms of a Ni–YSZ anode-supported cell operated sequentially in dry hydrogen (DH), cold recirculation of biogas before reformer (CB), and hot recirculation of biogas before reformer (HB). The study combines voltage monitoring, IV curves, electrochemical impedance spectroscopy (EIS), distribution of relaxation times (DRT) analysis, and complex nonlinear least-squares (CNLS) fitting to elucidate the evolution of anodic and cathodic processes under each fuel composition.

Voltage measurements reveal distinct stability windows for the three environments, with CB showing the largest voltage decay. DRT analysis identifies six electrochemical processes, whose relative contributions vary with fuel composition. CNLS fitting confirms that the Ni–YSZ interface retains its electrochemical activity throughout the test sequence.

Overall, this study provides a comprehensive interpretation of SOFC degradation under realistic biogas-derived fuels, highlighting that performance losses are primarily driven by gas-transport and cathodic polarisation processes, while the catalytic activity of Ni–YSZ anode remains largely preserved. These insights contribute to a clearer understanding of SOFC operation under renewable and pre-processed biogas feeds and provide guidance for future durability-oriented system design.

1. Introduction

Solid oxide fuel cells (SOFCs) are among the most promising electrochemical conversion technologies due to their high electrical efficiency, fuel flexibility, and capability for combined generation of power and heat at elevated temperatures [1]. Operating typically in the 700–850 °C range, SOFCs enable fast reaction kinetics and internal reforming, making them particularly attractive for the direct utilisation of hydrogen and even more of carbon-based fuels such as natural gas and biogas [2]. In the European context, the deployment of SOFCs for on-site energy conversion of biogas produced from agricultural residues and organic wastes represents a viable pathway to enhance the energy autonomy of small-scale farms, while simultaneously contributing to waste valorisation and decarbonisation targets [3,4].

Among commercially relevant architectures, Ni–YSZ anode-supported cells (ASCs) remain the most widely adopted due to their higher efficiency, the high catalytic activity of Ni for hydrogen oxidation, and the strong compatibility of the Ni–YSZ electrode with reforming processes under typical operating temperatures [5]. These features make Ni–YSZ ASCs particularly suitable for fuel-flexible operation, including hydrogen-rich reformates derived from biogas.

In recent years, several studies have explored cell performance under biogas or biogas-derived fuel mixtures [6], with particular attention to degradation mechanisms [7,8]. One major issue concerns carbon deposition, which can occur under carbon-rich or insufficiently oxidising conditions and lead to rapid performance decay due to the coverage of triple phase boundaries (TPBs), pore blockage, and Ni particle isolation.

Wu et al. [9] analysed the long-term stability and gradual degradation of Ni–YSZ ASCs fed with bio-syngas, identifying carbon deposition as the main driver of performance degradation. Lanzini and Leone [10] investigated SOFC operation under two simulated biogas feeds, namely

* Corresponding author.
E-mail address: hangyu.yu@epfl.ch (H. Yu).

https://doi.org/10.1016/j.electacta.2026.148838
Received 4 February 2026; Received in revised form 27 March 2026; Accepted 9 April 2026
Available online 10 April 2026

bio-methane and bio-hydrogen. Two cell types were tested: an anode-supported cell (Ni–YSZ) and an electrolyte-supported cell (3YSZ with a Ni-GDC anode). Pure bio-methane caused carbon deposition, which was mitigated by introducing oxidants such as air, steam, or CO_2, enabling direct internal reforming of methane. Instead of relying on internal reformer, Papurello et al. [11] integrated an external pre-reformer upstream of a short stack consisting of three anode-supported cells and investigated its degradation behaviour. With a H_2-to-CO ratio at around 2.5, the short stack presented an overall degradation rate below 0.5 %/kh over 500 h of operation.

A second critical issue concerns the complex interplay between H_2/CO/CO_2/H_2O equilibria and electrochemical kinetics [12], together with sulphur poisoning [13], which remains one of the most detrimental degradation mechanisms for Ni–YSZ anodes [14–16]. Sulphur-containing species such as H_2S strongly adsorb on Ni surfaces, suppressing hydrogen oxidation kinetics and inhibiting catalytic reactions such as the water–gas shift (WGS). Impedance-based studies by Weber et al. [17] revealed that sulphur contamination leads to a reduced electrochemical hydrogen oxidation rate and a deactivation of catalytic CO conversion via the water-gas shift reaction. Beyond sulphur, other trace contaminants commonly found in raw biogas have also been reported [18]. Papurello et al. [19] investigated the impact of a wide range of trace compounds on anode supported SOFC, showing that the worst-case degradation scenarios are associated with H_2S and the presence of D4 siloxane, even at ppb(v) level.

However, a notable lack of systematic studies remains regarding the long-term degradation behaviour and impedance response of Ni–YSZ anode-supported cells operated with pre-processed biogas. This operating regime is increasingly relevant for real-world deployment, as biogas is typically cleaned and conditioned to suppress coking and poisoning while stabilising fuel composition. Under such conditions, degradation is expected to be more subtle and progressive, making advanced state-of-health monitoring tools essentials. In particular, the combined interpretation of electrochemical impedance spectroscopy (EIS), distribution of relaxation times (DRT), and complex nonlinear least-squares (CNLS) fitting remains scarcely explored for pre-conditioned biogas environments.

The novelty of the present work lies in providing a detailed analysis of degradation mechanisms in a mature Ni–YSZ anode-supported cell operated under realistic, pre-processed biogas conditions. Unlike previous studies, this work does not focus on extreme poisoning or coking scenarios, but rather on how and where degradation develops when such risks are mitigated. Furthermore, two distinct biogas upgrading scenarios are compared, in which a fraction of the anode-off gas is recirculated upstream of an external reformer. The first scenario (CB) involves cold-drying of the recirculated anode off-gas, promoting dry reforming of methane and resulting in CO-rich reformate. The second scenario recirculates the moist off-gas, producing and H_2-rich reformate with lower energy density, so it is defined as hot biogas recirculation (HB).

To this aim, a commercial Ni–YSZ ASC is subjected to sequential long-term operation under dry hydrogen, cold biogas, and hot biogas recirculation feeds. Continuous voltage monitoring, IV characterisation, and EIS measurements are complemented by DRT analysis and CNLS fitting to deconvolute contributions from gas conversion, charge transfer, mass transport, and solid-state processes. By correlating resistance evolution, time constants, and dispersion factors across different fuels and current densities, this study provides new insight into the degradation pathways of fuel-flexible SOFCs and supports the development of more durable and reliable systems for biogas-based energy generation.

2. Experimental setup

2.1. Test bench and cell configurations

The test station is equipped with advanced components to enable precise operation and monitoring. The cell is mounted in a Rohde top-loaded furnace, and gas supplies are controlled by mass flow controllers (MFC, Bronkhorst, F-201CV series), while a peristaltic pump (Ismatec, Reglo ICC) is used for water injection. An open-close configuration, combined with a glass sealant, ensures gas tightness at the anode and prevents leakage between the cell and the metallic flange. The anode is contacted with a Ni foam and a gold mesh contacts the cathode, each electrode having separate current and potential wires, which are twisted to cancel out wire induction and improve the quality of high-frequency impedance measurements.

Further details on the experimental setup for SOFC operation are provided by Moussaoui et al. [20] and can be found in a previous work by the authors [8].

The cell manufactured by SolydEra is characterised by a circular active area of 12.56 cm^2 and exhibits the following five-layer functional structure: Ni–YSZ/8YSZ/GDC/LSCF-GDC/LSC (Table 1). The thick, porous anode has a thickness of 260 µm and serves as both the functional layer and structural support, while the electrolyte is 10 µm thick ($(ZrO_2)_{0.97}(Y_2O_3)_{0.03}$). The electrolyte is followed by a 1 µm GDC barrier layer situated between the cathode and the electrolyte, suppressing detrimental chemical reactions and interdiffusion between LSCF and YSZ at operating temperatures. The cathode consists of an LSCF-GDC composite with a thickness of 15 µm, followed by an LSC air support layer.

2.2. Test protocols

The cell is initially heated from room temperature to 855 °C at a controlled rate of 100 °C/h, while supplying N_2 to the anode and air to the cathode side. Once the target temperature is reached, the glass sealant is sintered in situ to guarantee gas-tight operation; subsequently, the temperature is reduced to 800 °C. The reduction of NiO to metallic Ni is then carried out by supplying a 60/40 vol% H_2/N_2 gas mixture to the anode, for a minimum duration of 12 h. This step ensures full activation of the Ni-based anode before initiating long-term electrochemical testing.

Durability tests are subsequently performed under three distinct gas compositions: dry H_2, CB and HB. These specific gas mixtures are selected to reproduce environments representative of real SOFC operating conditions, including both ideal (dry H_2) and biogas-derived atmospheres. The gas compositions are selected based on partner research [21–25], in which carbon deposition was avoided. The complete gas compositions are reported in Table 2.

At the anode, two main reactions occur:

(1) hydrogen oxidation, producing steam according to:

$$H_{2(g)} + \frac{1}{2}O_{2(g)} \rightarrow H_2O_{(g)} \quad \Delta H_{298K} = -241.8 \text{ kJ} \Big/ \text{mol} \tag{1}$$

and (2) the water gas shift:

$$H_2O_{(g)} + CO_{(g)} \rightarrow H_{2(g)} + CO_{2(g)} \quad \Delta H_{298K} = -41.2 \text{ kJ/mol} \tag{2}$$

These reactions dominate the electrochemical environment at the anode and are strongly influenced by the selected gas mixtures.

The experimental campaign focuses on real-time electrochemical monitoring, aimed at assessing degradation behaviour during long-term operation under polarised conditions. All tests are carried out on the

Table 1
Material and thickness of cell layers.

Layer	Layer material	Thickness
Fuel functional layer	Ni–YSZ	260 µm
Electrolyte layer	8YSZ	10 µm
Barrier layer	GDC	1 µm
Air functional layer	LSCF-GDC	15 µm
Air support layer	LSC	15 µm

Table 2
Operating conditions of the test conducted, including fuel utilisation (FU), air utilisation (AU), total inlet gas flow rates, and inlet gas composition at the anode and cathode.

	Anode								Cathode		
	FU [%]	H_2 [%]	CO [%]	CO_2 [%]	H_2O [%]	CH_4 [%]	N_2 [%]	Flow [sccm]	AU [%]	Air [%]	Flow [sccm]
DH	77.8	60	-	-	-	-	40	75	17	100	490
CB	32.5	21	39	29	10	1	-	168.42	17	100	490
HB	42.5	40	33	14	11	2	-	101.76	17	100	490

same single cell, which is sequentially exposed to DH, CB, and HB environments while maintaining constant parameters such as temperature, air-electrode flow rate, and a fixed current density of 0.4 A·cm^{-2}. Fig. 1 shows the exposure times for DH, CB, and HB, which are 262 h, 258 h, and 231 h, respectively, for a total test duration of nearly 750 h. These different time intervals were selected to reflect the cell stability under each gas composition and to ensure that representative levels of degradation and quasi-stable regime are reached before transitioning to the next condition, allowing a meaningful comparison of the changes induced by fuel switching while minimizing cell-to-cell variability. The duration of each step is also adjusted in accordance with laboratory scheduling and working-day constraints, which impose practical limits on continuous operation.

For each gas composition, cell performance is assessed through a combination of voltage tracking, IV characterisation, and electrochemical impedance spectroscopy. After stabilisation of the open-circuit voltage (OCV) under the new gas mixture, IV curves are recorded at a scan rate of 1 mV/s from OCV down to 700 mV. These measurements are followed by EIS at both full (0.4 A·cm^{-2}) and half (0.2 A·cm^{-2}) current density. Impedance spectra are collected using $a \pm 200$ mA sinusoidal perturbation, sweeping the frequency range from 200 kHz to 20 mHz with ten logarithmically spaced points per decade. At the end of each durability stage and prior to switching to the next gas composition, the same IV and EIS protocols are repeated. This approach enables direct comparison with the initial state in each atmosphere and allows quantification of the incremental degradation induced by the operating conditions.

3. Data analysis

Data are treated by using the open-source software SOCEIS. To ensure the reliability of the impedance spectra, the raw EIS data are first subjected to a validation and cleaning procedure based on the linear Kramers–Kronig (KK) method, following the methodology detailed in the author's earlier work [8]. Mid-frequency anomalies, often originating from periodic disturbances such as the 50 Hz electrical grid, are identified and removed. After eliminating these outliers, the spectra are smoothed and extended using KK-based extrapolation to obtain a consistent dataset suitable for further analysis.

The distribution of relaxation times (DRT) is then reconstructed by applying Tikhonov regularisation. The acceptable range of regularization parameter was first identified using the L-curve criterion. The final value $\lambda = 0.01$ was then selected as a compromise between the optimal values suggested by the different spectra and the practical need for stable and comparable deconvolution across all operating conditions. The same value was then applied consistently to all spectra to preserve comparability among the different fuel environments and operating conditions.

These DRT profiles provide the basis for selecting the number and type of RQ elements required in the equivalent circuit model (ECM), ensuring that each electrochemical process could be resolved individually, as illustrated in Fig. 2. With the ECM architecture established, a complex nonlinear least-squares optimisation is performed to extract the characteristic resistances, time constants, and dispersion factors associated with each identified process.

4. Results and discussion

4.1. Current and voltage characterisation

Fig. 3 and Table 3 present the voltage evolution over time at a current density of 0.4 A cm^{-2} under the three operating environments: dry hydrogen (DH), cold biogas recirculation before the reformer (CB), and hot biogas recirculation before the reformer (HB). Each stage includes an initial stabilisation period; therefore, the voltage values discussed correspond to the steady-state regime, defined as the interval in which

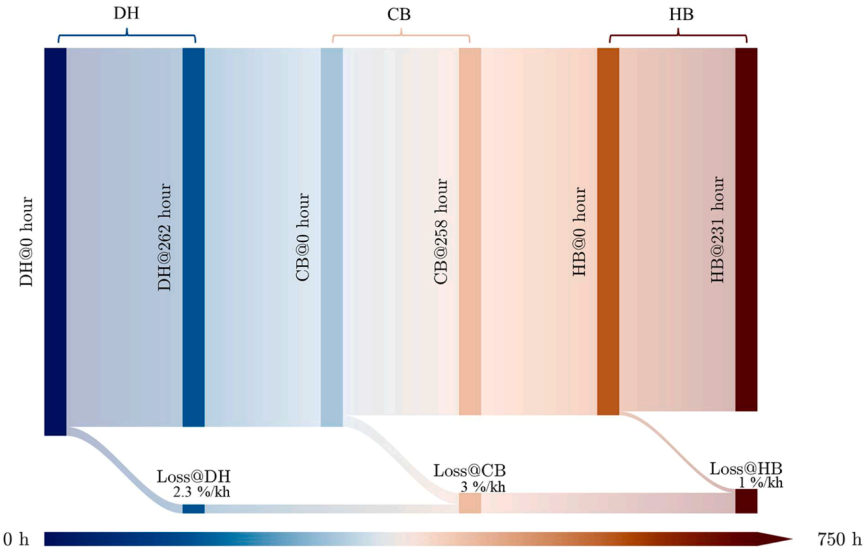

Fig. 1. Timeline of degradation tests. The connecting curves represent the degradation rates, expressed as percentage loss per kilohour (%·kh^{-1}).

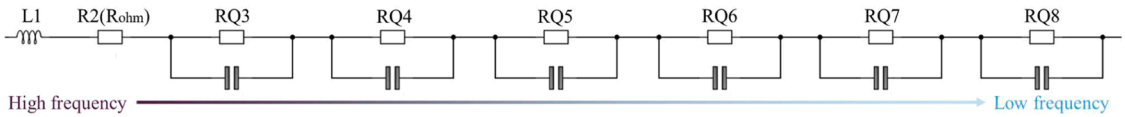

Fig. 2. Equivalent circuit model consisting of one inductor (L1), one resistor (R2), six RQ elements, where the bigger number corresponds to the lower frequency process.

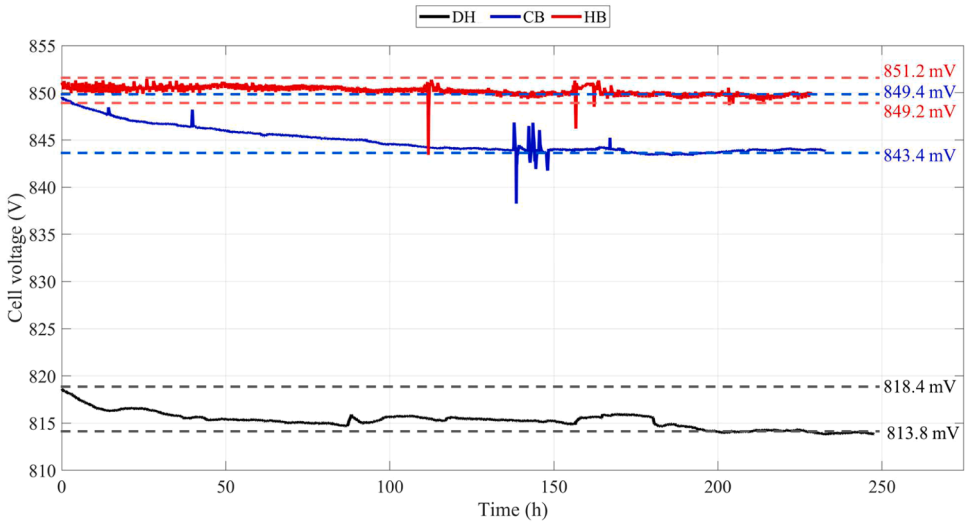

Fig. 3. Voltage degradation under different gas compositions at a current density of 0.4 A·cm^{-2}.

Table 3
Voltage measurements under different gas compositions.

	OCV	Initial	End	Degradation rate	
	[mV]	[mV]	[mV]	[mV/kh]	[%/kh]
DH	1156	818.4	813.8	18.6	2.3
CB	994	849.4	843.4	25.8	3.0
HB	1023	851.2	849.2	8.73	1.0

the time derivative of the voltage approaches a constant value.

Under DH operation, the cell needs a stabilisation period typically attributed to the progressive activation of the Ni–YSZ anode once the reducing atmosphere is fully established and the triple-phase boundaries become electrochemically active. In addition, voltage variations can be associated with microstructural rearrangements, residual sealant consolidation, and initial degradation of the electrode/electrolyte interface. Beyond this transient phase, the voltage stabilises and reaches a final value of 813.8 mV, indicating that the cell enters a quasi-steady degradation regime.

When operating under CB conditions, the voltage exhibits a gentler evolution. A gradual decrease is observed during the first hours of operation, corresponding to a total loss of approximately 7 mV. This early-stage decay reflects the combined effects of lower H_2 partial pressure and the presence of CO and CO_2, which modify both the reaction kinetics and the local gas composition through the water-gas shift equilibrium. After this transient, the cell voltage decreases slowly, stabilising at 843.4 mV and displaying a relatively stable long-term performance under CB composition. Notably, the overall voltage remains higher than under DH, despite the lower fuel quality. This behaviour is mainly attributed to the lower effective fuel utilisation under CB conditions (FU from 77.8 in DH to 32.5 in CB), which limits local hydrogen depletion and concentration overpotentials, while WGS-mediated hydrogen regeneration further stabilises the anode potential.

In contrast, operation under HB leads to a negligible voltage decrease during the initial hours, reflecting the thermochemical and kinetic impact of the HB biogas composition. Following this decline, the voltage enters a stable plateau with minimal fluctuations, resulting in a total voltage loss of only 3 mV over the 231 h test period. This behaviour suggests that the anode rapidly equilibrates under HB conditions and then operates in a remarkably steady regime, possibly due to enhanced reforming kinetics at high temperature.

Overall, the three profiles reveal distinct transient and steady-state behaviours, indicating that the dominant degradation mechanisms and their time constants differ substantially across DH, CB, and HB environments. Although the HB stage exhibited the lowest measured degradation rate in the present campaign, this result must be interpreted with caution. Since the durability tests were carried out sequentially on the same cell, the HB exposure was reached only after prolonged prior operation under DH and CB. Therefore, the lower degradation rate observed under HB may partly reflect the progressive stabilization of the ageing behaviour of the cell, rather than an intrinsically lower degradation severity of the HB environment itself.

The present results can be directly compared with the electrolyte-supported NiO-GDC/GDC/3YSZ/GDC/LSCF cell investigated by Yu et al. [26], who also analysed durability under sequential DH-CB-HB-DH operation by means of IV curves, EIS, DRT, and CNLS fitting. In both studies, the CB environment leads to the highest voltage degradation. However, in the present work the lowest degradation rate corresponds to the HB environment, in contrast to the previous study, where the lowest degradation rate was observed under dry hydrogen.

Fig. 4 presents the voltage-current density and corresponding power density curves recorded at the beginning and end of each durability stage. Based on the current density at 700 mV, the CB case shows the best performance, reaching the highest current density. However, cold biogas operation also results in the most significant performance decay. While the OCV remains stable, the voltage under load decreases noticeably after 258 h, leading to a reduction in both the cell electrochemical efficiency and maximum power output. The more pronounced drop in the medium and high current density regions of the IV curve suggests the combined effects of increased anode polarisation and

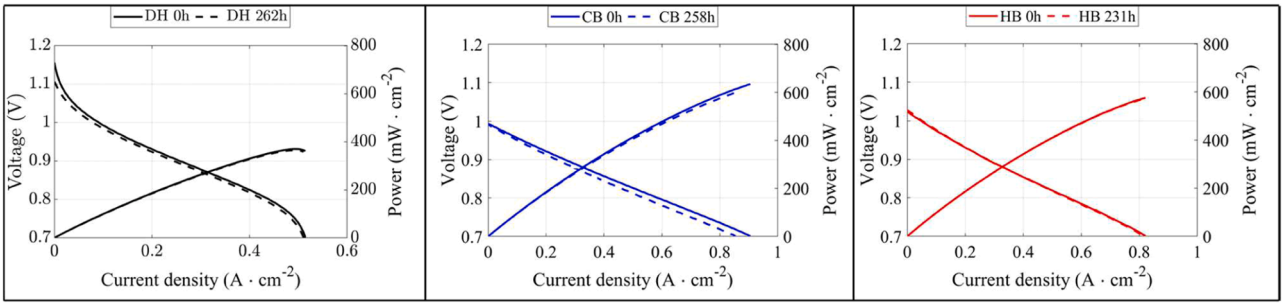

Fig. 4. Current–voltage characterisation and power production under different gas compositions.

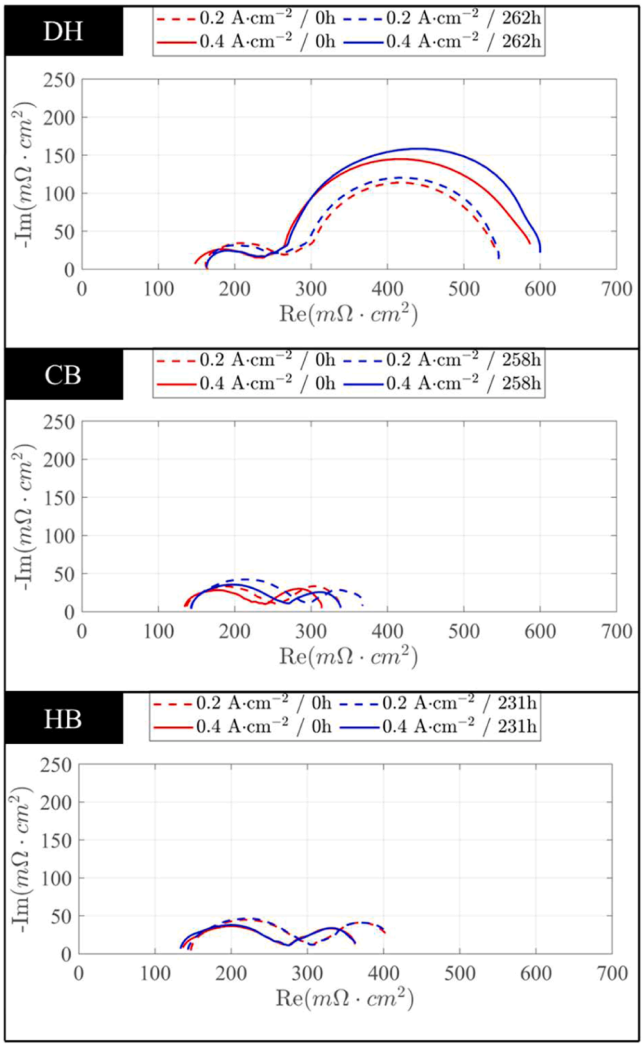

Fig. 5. Nyquist plot of normal degradation under dry hydrogen (DH) in the beginning, CB environment, and HB environment. Solid line represents the case with full current density and the dashed line represents the case with half current density.

modest contributions from mass-transport limitations, consistent with the complex $H_2/CO/CO_2/H_2O$ equilibria present in CB mixture.

Under HB conditions, the IV and power curves at 0 h and after 231 h practically overlap, showing that the cell performance is remarkably stable in this fuel, as already observed from the voltage trend over time. Neither the OCV nor the voltage under load exhibit a significant shift, and the maximum power density is preserved within experimental scatter. This indicates that, under the present operating conditions, HB does not introduce additional performance decay compared with the beginning of the test stage.

4.2. *Electrochemical impedance spectroscopy*

The Nyquist plots obtained under the different operating conditions are shown in Fig. 5. For each condition, impedance spectra are collected at two current densities, 0.2 and 0.4 A·cm^{-2}, both at the beginning of the stage and before switching the gas composition. This approach allows a direct comparison of the degradation behaviour associated with each gas environment.

Under the first DH stage, the cell exhibits the largest impedance arcs among the three conditions, reflecting the highest overall polarisation

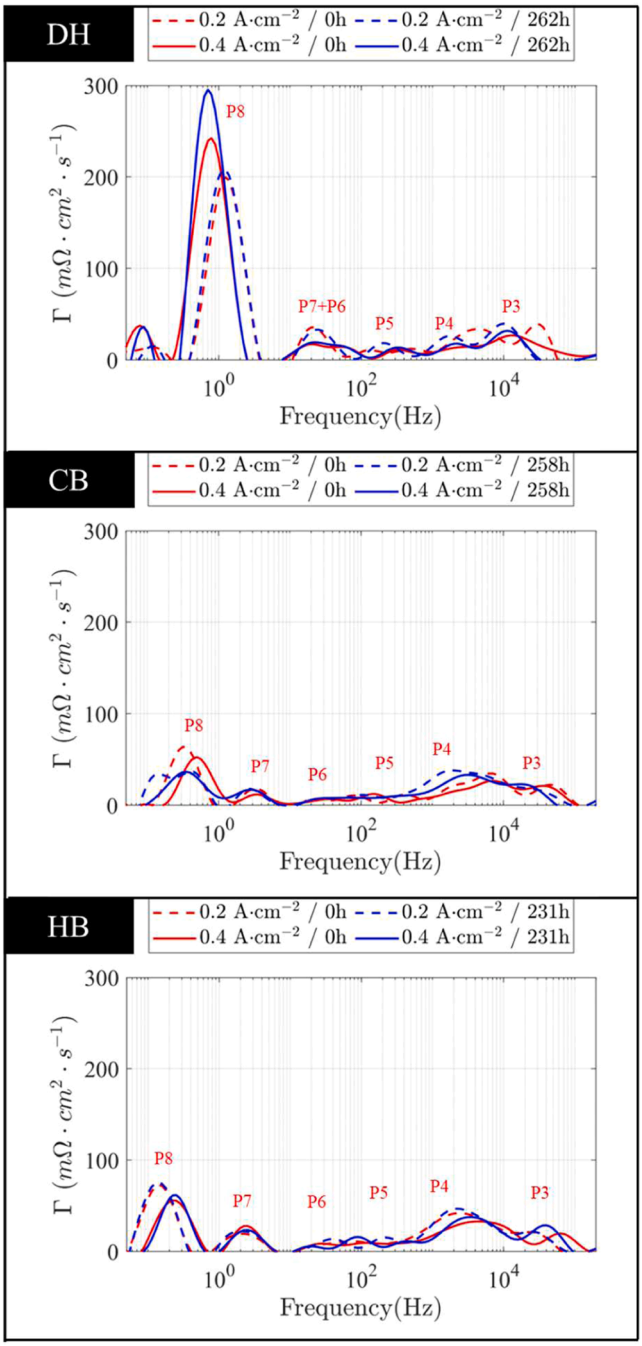

Fig. 6. DRT results with peak recognition to compare the behaviour of different gas composition. All measurements are taken before and after switching the gas composition. The solid line represents the case with full current density, while the dashed line represents the case at half current density.

resistance. At 0.4 A·cm^{-2}, the diameter of the main arc increases markedly from the beginning to the end of the DH period. This increase is consistent with the decreasing voltage trend already observed in Fig. 3. The high-frequency intercept remains relatively unchanged, suggesting limited ohmic degradation.

When switching to CB, the impedance is substantially reduced compared with DH. The arcs become smaller and flatter, particularly at 0.4 A·cm^{-2}, indicating enhanced reaction kinetics. This behaviour can be attributed to the presence of CO and CO_2, which shifts the local equilibrium through the water-gas shift reaction, increasing the in-situ H_2 partial pressure at the anode. The shape of the Nyquist plot evolves from a small high-frequency arc and dominant low-frequency arc (DH) to a multi-arc structure with a more pronounced mid-frequency feature. This is commonly associated with gas conversion processes (CO/H_2 reforming) and surface exchange kinetics. The increase in impedance between the initial and final CB measurements is modest, showing limited degradation during this period.

Compared with CB, the HB spectra exhibit slightly larger high-frequency resistance, and the overall polarisation is a bit higher. The difference between the initial and final HB measurements is minimal, indicating that the cell experiences very limited additional degradation in this environment over the 231 h test period.

4.3. Distribution of relaxation times

DRT results are shown in Fig. 6 for the three cases (DH, CB, and HB). Six characteristic peaks are consistently observed, each corresponding to a specific electrochemical process. The attribution of each peak (see Table 4) has been given starting from the work of Caliandro et al. [27] and further supported by previous SOFC impedance studies reported in literature [28,29]. In this work, the DRT peaks are labelled from P3 to P8 in order to preserve direct consistency with the numbering of the equivalent-circuit elements used in the CNLS fitting (L1, R2, RQ3–RQ8).

The lowest-frequency peak (P8) is linked to gas conversion at the fuel electrode, as it shows the largest variation when switching the fuel composition. A weak additional feature is visible at the lowest frequencies under DH conditions. Because it lies close to the lower boundary of the measured frequency window, its interpretation remains uncertain. It may partly arise from low-frequency noise or external perturbations (e.g. flow or pressure fluctuations) as can be observed in Fig. A.1. In addition, Tikhonov-regularized DRT reconstruction can generate secondary sub-peaks when deconvolving a broad low-frequency. In the intermediate-frequency region (1–50 Hz), peaks P7 and P6 are difficult to distinguish in DH, especially at full current density, and are likely convoluted. These contributions are attributed, respectively, to fuel-electrode gas-diffusion resistance, which is affected by the WGS reaction (P7), and to oxygen-electrode surface reaction (P6). Their merging under DH may reflect a coupling between hindered fuel transport, expected when hydrogen concentration is high but water formation is rapid, and an increased oxygen-electrode reaction resistance as polarisation builds up. At higher frequencies, the P5, P4, and P3 contributions, associated with oxygen-electrode transport and oxygen charge transfer (50–500 Hz), fuel-electrode charge transfer (0.5–5 kHz), and solid-state process (>5 kHz), respectively, show comparatively limited sensitivity to changes in fuel composition. This indicates that while the gas-phase composition significantly influences low- and mid-frequency mass-transport and conversion processes, charge transfer processes remain relatively stable across the tested mixtures.

Overall, the behaviour of the six DRT peaks underscores the dominant role of gas-conversion and diffusion phenomena in controlling

Table 4
Peaks classification for different electrochemical processes, where P2 and P1 are associated with the ohmic resistor and inductor, respectively.

	P8	P7+P6	P5	P4	P3
Process	Gas conversion	Fuel electrode diffusion and oxygen electrode reaction	Oxygen electrode transport and oxygen charge transfer	Fuel electrode charge transfer	Solid state process
Frequency	0.1–1 Hz	1–50 Hz	50–500 Hz	0.500–5 kHz	>5 kHz
Related electrodes	Anode	Anode and cathode	Cathode	Anode	Electrolyte

impedance under diluted or reformed fuels, while high-frequency reaction steps are primarily governed by electrode material properties rather than inlet composition.

4.3.1. Impact of current density

Because only two representative current densities were investigated (0.2 and 0.4 A/cm^2), the following discussion should be interpreted as a comparison between half-load and full-load operating conditions rather than as a generalized current density trend.

Fig. 6 shows that under DH, gas conversion (P8) is more pronounced with current density due to a higher rate of H_2 consumption and H_2O production at the TPB, which amplifies concentration gradients in the absence of inlet steam. In contrast, under CB and HB, the inlet fuel already contains significant amounts of H_2O, CO, and CO_2, and gas conversion involves multicomponent equilibria, mainly governed by the water-gas shift reaction. Under these conditions, increasing the current density does not amplify concentration gradients to the same extent. Instead, the buffering effect of steam and carbon-containing species stabilises the local gas composition, resulting in a reduced P8 amplitude and a shift toward higher frequencies when moving from 0.2 to 0.4 A·cm^{-2}. Intermediate-frequency processes show a more moderate sensitivity to current density. Peaks P6 and P7 exhibit only limited changes with increasing current density, indicating that these processes are primarily governed by intrinsic material properties rather than by operating load. Similarly, the charge-transfer-related peaks P4 and P5 decrease in amplitude with increasing current density, while their relaxation frequencies shift to higher values, reflecting faster electrochemical kinetics under higher polarisation. Among these, only P4 shows a clear dependence on the fuel side, whereas P5 remains largely insensitive to changes in current density. At the highest frequencies, the solid-state peak P3 remains essentially unchanged between the two current densities, confirming that bulk transport and purely solid-state processes are not affected by variations in electrochemical load.

A quantitative comparison of the fitted resistance values is provided in the CNLS section and summarized in Table S. 1.

4.3.2. Impact of gas composition

As shown in Fig. 6, at the end of the test in DH, the DRT is dominated by a pronounced low-frequency peak (P8) centered at 0.5–1 Hz. The peak related to the gas conversion resistance (P8) is much higher in DH than in CB or HB. This is attributed to the absence of H_2O in the DH feed, which leads to a stronger perturbation of the local H_2/H_2O ratio at the TPB. Under dry hydrogen, even small changes in current density induce large variations in local gas composition, leading to a dominant gas-conversion response. In CB, the presence of H_2O together with CO and CO_2, partially buffers the gas-phase composition through water gas shift reaction, thereby reducing the amplitude of the gas-conversion response. As a consequence, the gas-conversion resistance becomes less sensitive to current density in CB. Also in the Ni-GDC ESC case [26], the presence of steam in CB strongly reduces the gas-conversion resistance compared to dry hydrogen. The evolution of the impedance parameters indicated that the major degradation stemmed from increased resistances associated with oxygen surface exchange and ohmic losses. Gas-conversion and surface-exchange resistances were notably affected by environmental conditions.

Moving from CB to HB (Fig. 6), a slight increase in P8 is observed. This difference can be rationalised by the higher fuel utilisation and lower total fuel flow in HB compared with CB (see Table 2). Under HB, a given current perturbation induces a larger relative change in the local fuel composition at the anode, making the gas-conversion process more visible in the DRT spectra, despite the continued buffering effect of H_2O, CO, and CO_2.

In the medium-frequency region (1–50 Hz), corresponding to combined anode diffusion and cathode surface processes, DH also displays a higher amplitude compared to CB. Under biogas reformates, peaks P6 and P7 become better resolved: P7 shifts toward lower frequencies, leading to partial deconvolution from P6. This behaviour reflects the modified gas environment and altered surface exchange dynamics induced by steam and carbon-containing species. P7 appears slightly slower and more pronounced in HB than in CB, while remaining largely independent of current density.

At higher frequencies (>10^3 Hz), all curves nearly collapse, indicating that the related processes (charge transfer and solid-state contributions) are weakly affected by switching from DH to CB.

An evolution occurs in the low-frequency region when comparing the DRT spectra of dry hydrogen at the beginning and HB at the end of the long-term test (Fig. A.2c). After 750 h of operation, P8 decreases in amplitude and simultaneously shifts toward lower frequencies. This behaviour indicates that the gas conversion process becomes less dominant and faster in its characteristic response. Such a trend is consistent with fuel composition and the cell history, rather than a severe degradation of the Ni–YSZ anode. After exposure to CB and HB, the anode operates with a partially aged but still catalytically active microstructure and with some residual steam in the anode compartment, which buffers the gas composition and reduces the amplitude of the gas-conversion response with respect to the beginning of the test, even though the underlying resistance remains of the same order of magnitude.

4.4. CNLS fitting

CNLS fitting is employed to quantify the parameters of each element of the equivalent circuit (i.e., the inductance, resistances, relaxation times, and dispersion coefficients), and to study their evolution with time while the cell is operated under different conditions. As indicated in Fig. 2, six RQ elements are applied to represent different processes (see Table A.1 for the probability values associated with the fitting).

4.4.1. Resistance variations

Fig. 7 summarises the resistance trends for both half and full current densities. Notably, as already seen in Fig. 6, the gas conversion resistance (RQ8) exhibits its highest values under DH because the higher FU

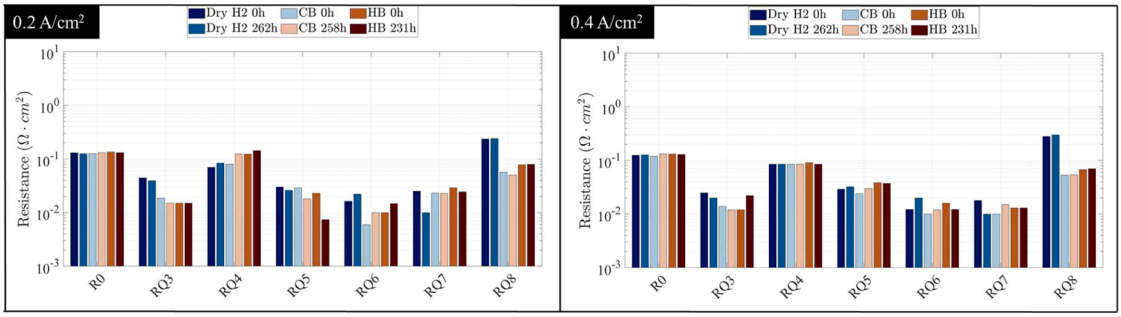

Fig. 7. Resistance of different elements for case with half current density and full current density.

and the absence of inlet steam amplify the H_2/H_2O concentration gradients generated by the electrochemical reaction. As a result, local gas composition becomes highly sensitive to current, increasing the associated impedance at full current density. In contrast, both CB and HB show a decreased resistance, as clarified in the DRT plots. The gas mixture buffers the TPB composition, reducing the perturbation of the local gas composition and leading to a lower gas-conversion resistance. RQ8 is lowest under CB conditions, benefitting from lower fuel utilisation and a higher contribution of the water–gas shift reaction due to the higher CO content, both minimising pH_2 and pH_2O gradients.

On the other hand, the resistances associated with RQ7 and RQ6, which describe the intermediate-frequency processes combining fuel-electrode diffusion and oxygen-electrode surface reaction, exhibit comparatively modest variations across the different fuel compositions. It is worth noting that, as already mentioned, although RQ7 is primarily associated with diffusion-dominated processes, RQ6 is also assumed to include a partial contribution from fuel-side gas diffusion, in addition to the oxygen-electrode reaction component. Under dry hydrogen, RQ7 and RQ6 evolve differently over time: RQ7 shows a gradual decrease, whereas RQ6 increases for both current densities. This opposite trend suggests a redistribution of the dominant intermediate-frequency processes as degradation progresses. The decrease in RQ7 does not imply an intrinsic improvement of gas diffusion; instead, it is attributed to changes in the effective reaction zone and current distribution within the porous anode. In addition, for reformate-containing fuels, an additional contribution may arise from multicomponent diffusion involving both H_2 and CO, together with water-gas shift reactions catalysed on nickel within the anode structure. These coupled processes can locally buffer fuel composition and modify the effective diffusion pathways, influencing both the resistance and the dispersion behaviour. In contrast, the slight increase in RQ6 with current points to a growing contribution from the faster component of the process, which includes both residual gas-transport effects and oxygen-electrode surface kinetics. Since the operating conditions of the air electrode are kept constant and only the fuel composition is varied, the degradation observed in RQ6 is attributed to the general ageing of the cell during long-term operation, rather than to fuel-specific chemical effects.

The resistance associated with RQ5, attributed to oxygen-electrode transport and charge-transfer processes, exhibits a similar behaviour at the two current densities. RQ5 remains almost constant for all gas compositions and times, indicating that ageing effects and subtle changes in gas composition have little impact on the resistance measured by EIS.

The fuel electrode charge transfer resistance (RQ4) remains nearly unchanged across different environments. Charge transfer resistance increases only when the TPB shrinks [30,31] due to nickel coarsening, carbon deposition, sulphur contamination [18] or severe redox damage.

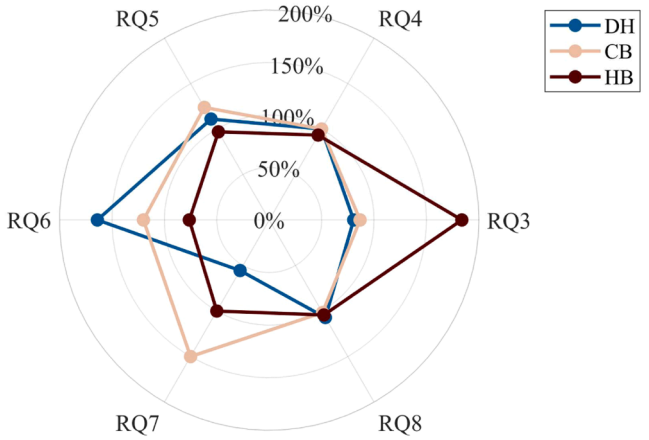

Fig. 8. Percentage variation of resistances for case with full current density.

In our test, the biogas composition has been chosen to avoid any carbon deposition, sulphur is not present and no redox cycling occurs. Hydrogen charge-transfer kinetics at the Ni–YSZ TPB remain fast for the entire range of H_2 partial pressures used, and $CO/CO_2/H_2O$ do not directly affect the intrinsic electrochemical reaction.

Furthermore, post-mortem SEM analysis was performed by the Schottky Field Emission SEM after the durability campaign, which did not reveal evidence of severe microstructural degradation (see Supplementary material). In particular, no delamination, no damaged interfacial regions between layers, and no loss of adhesion between the electrolyte and the anode were observed, while the porous microstructure of both electrodes remained preserved. These observations are consistent with the nearly unchanged RQ4 values and support the conclusion that no significant TPB degradation occurred under the tested conditions.

The resistance associated with RQ3, assigned to the solid-state process, decreases with current density and shows modest variations across the different gas compositions and test durations. This behaviour is expected because RQ3 reflects processes that occur within the solid components of the cell, which are fundamentally insensitive to changes in the anode gas composition. Unlike gas conversion or diffusion-related mechanisms, solid-state transport is governed by microstructural and material properties rather than by the external fuel feed. Ohmic resistance remains stable for both current densities.

Overall, the resistance analysis highlights that the fuel composition primarily affects gas-related and intermediate-frequency processes, while intrinsic electrochemical and solid-state mechanisms remain largely stable, confirming that neither the Ni–YSZ TPB nor the bulk cell components undergo significant degradation under the selected pre-processed biogas compositions.

4.4.2. Degradation

Fig. 8 presents the percentage increase of the resistance associated with each RQ element relative to the beginning of each test stage (DH, CB, HB) at full current density. The radar plot highlights how degradation and time operation affect the various electrochemical processes differently depending on the gas composition.

The largest increase is observed with DH for RQ6, which represents oxygen electrode reaction. This variation is consistent with degradation mechanisms commonly reported for Ni–YSZ cells operated for long durations. As highlighted by Lyu et al. [32], cathode degradation can arise from both microstructural and chemical evolution at the oxygen electrode. In particular, the gradual formation of oxygen-blocking surface phases (e.g., O^{2-}-inhibiting layers on the electrolyte surface) has been shown to significantly increase the oxygen conduction resistance, contributing up to ~40 % of the overall performance decay in long-term tests. RQ6 for other fuels is increasing with a slower rate. It should be noted that RQ6 is assumed to include a partial contribution from gas-phase diffusion phenomena, overlapping with those represented by RQ7. Given that RQ6 and RQ7 are partially convoluted in the DRT spectra, particularly under DH conditions, it is more appropriate to consider the combined variation $\Delta(RQ6 + RQ7)$ as a measure of the overall degradation of intermediate-frequency processes. When evaluated in this manner, the results indicate a moderate but systematic degradation during long-term dry hydrogen operation.

Under CB conditions, the resistance associated with RQ7 increases during operation. In this case, the presence of H_2O and CO_2 reduces the effective hydrogen diffusivity and alters the gas-phase composition within the porous anode, thereby reinforcing mass-transport limitations. Under HB, the higher hydrogen content mitigates this effect, leading to an almost negligible increase in RQ7.

By contrast, RQ8, RQ5 and RQ4, associated with the gas conversion, oxygen electrode transport and fuel electrode charge-transfer processes, respectively, remains relatively unchanged across all conditions. This suggests that the Ni–YSZ interface retains its catalytic activity, and no major degradation mechanisms (e.g., sulphur poisoning or nickel

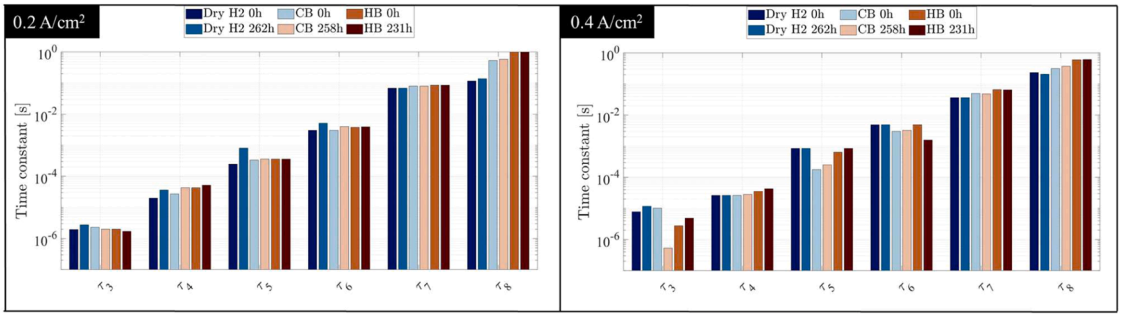

Fig. 9. Time constant of different elements under different gas environment for case with half current density and full current density.

coarsening) are active under the tested reformate compositions.

RQ3 remains almost unchanged during DH and CB operation, a slight increase is observed in HB, which could be caused by microstructural and material properties changes as previously discussed.

Overall, the resistance evolution indicates that the degradation is mainly concentrated in the intermediate-frequency processes associated with the oxygen-electrode related phenomena and diffusion, with RQ6 and the partially overlapping RQ7 representing the dominant source of long-term performance decay. These findings demonstrate that, under realistic biogas operation, long-term degradation is governed primarily by cathode-related and intermediate-frequency mechanisms rather than by fuel-side poisoning or irreversible anode damage.

4.4.3. *Time constant*

Fig. 9 compares the characteristic time constants (τ) of the different electrochemical processes identified through CNLS fitting for both 0.2 $A{\cdot}cm^{-2}$ and 0.4 $A{\cdot}cm^{-2}$ operating conditions. Each bar cluster corresponds to a specific RQ element under the three gas environments, presented both at the beginning and at the end of each exposure period.

Across all operating conditions, the time constants follow the expected frequency hierarchy of electrochemical processes, starting from the RQ3 exhibiting the shortest τ values (10^{-6}–10^{-5} s), followed by τ_4-τ_7 (10^{-5}–10^{-2} s), and finally RQ8, which has longest τ values (10^{-1}–10° s). This hierarchy confirms the robustness of the fitting and the correct physical assignment of the processes.

A clear and systematic increase of τ_8 is observed when transitioning from DH to CB and HB for both current densities (DH<CB<HB). This trend reflects the increasing complexity of the gas composition. Under DH, gas conversion mainly involves the H_2/H_2O equilibrium in a H_2/N_2 mixture, enabling rapid re-equilibration of the local gas composition near the anode, giving the smallest τ_8. In CB and HB, the fuel contains significant fractions of H_2O, CO, CO_2 and traces of CH_4. Gas conversion therefore involves a multicomponent mixture and is coupled to homogeneous chemistry, in particular the water-gas shift equilibrium. These factors slow down the relaxation of local gas composition in the porous anode and lead to larger τ_8 values for CB and HB, in agreement with trends observed in the DRT spectra (Fig. A.1).

Notably, τ_8 is generally larger at half current density than at full current density, except in DH, where gas conversion is intrinsically faster. The higher current density enhances reactant consumption, steepens concentration gradients, and accelerates local equilibration, which can effectively reduce the apparent time constant.

The time constants associated with RQ7 remain nearly unchanged across all fuels and currents, indicating that the combined process of fuel-side diffusion and oxygen-electrode reaction is only weakly sensitive to gas composition. For RQ6 and RQ5, time constants tend to decrease slightly under CB and HB. A plausible explanation is that biogas mixtures create a different local gas-phase environment, more oxidising and with lower H_2 diffusivity, which modifies the characteristic diffusion length or reaction balance, making the associated relaxation marginally faster. In addition, the WGS reaction could alter the local thermal field, increasing the effective temperature of the cell. The temperature rise can accelerate oxygen exchange kinetics, lowering τ_5.

Time constant τ_4 shows a very slight increase, having DH<CB<HB at both current densities, accordingly to DRT plots. This can be explained by the change in gas composition, which makes the process a bit faster as mentioned for τ_8.

At half current density, solid-state time constant τ_3 increases slowly with CB and HB, while at full current density the trend is not clear. This weak sensitivity is expected, as τ_3 is governed by material properties (ionic/electronic conduction, interface polarisation) rather than gas composition. Small variations may be attributable to temperature fluctuations, local stoichiometry changes, or evolving microstructure during long-term operation.

When comparing 0.2 $A{\cdot}cm^{-2}$ to 0.4 $A{\cdot}cm^{-2}$, τ tends to decrease slightly for most processes. Higher current densities generally increase reaction rates and amplify electrochemical driving forces, which accelerate electrochemical dynamics. The effect is most evident at high frequencies, where charge-transfer kinetics dominate and respond directly to increased polarisation.

Overall, the time constants remain remarkably stable over time within each gas composition, indicating that: (1) Degradation primarily affects the magnitude (R) of the processes rather than their intrinsic kinetics (τ); (2) the underlying mechanisms remain active and unchanged, even as microstructural or chemical deterioration increases the resistance.

The dispersion factors (α) associated with the RQ elements are reported in Fig. A.2. No systematic trends attributable to fuel composition or degradation time are observed, suggesting that long-term operation mainly affects the magnitude (R) and characteristic timescale (τ) of the processes, rather than their degree of dispersion. Some fitted dispersion factors approach the imposed lower bound ($\alpha = 0.4$), particularly under dry hydrogen and, to a lesser extent, under cold biogas conditions. A low α value reflects a highly dispersed response, indicating that the corresponding impedance contribution does not originate from a single, well-defined relaxation process but rather from a broadened distribution of time constants. Such dispersion can arise from overlapping electrochemical phenomena, spatial heterogeneities within the porous electrodes, and experimental noise affecting specific frequency ranges.

In particular, the dispersion factor is sensitive to local scatter in the impedance data. To ensure physically meaningful fits while maintaining numerical stability, α is constrained between 0.4 and 1. Values reaching the lower bound therefore indicate that the experimental data would favour an even broader distribution than the model allows, rather than a good quality of the fit. This interpretation is supported by the comparison between truncated experimental data and fitted spectra (Fig. A.3), which shows an excellent agreement between model and data despite the presence of a limited number of dispersed points.

Importantly, although the dispersion factor may be affected by measurement noise and process convolution, the extracted resistances and characteristic time constants remain stable and consistent across repeated fits and operating conditions. This confirms that the fitting

strategy prioritises an accurate representation of the impedance magnitude and timescale over enforcing artificially sharp arcs, thereby ensuring robust interpretation of resistance evolution and degradation mechanisms.

5. Conclusions

This paper focused on the study and test of an anode supported cell composed of Ni–YSZ/8YSZ/GDC/LSCF-GDC/LSC, which operated under 3 different gas compositions: (1) Dry hydrogen 60 % H_2 + 40 % N_2, (2) CB 21 % H_2 + 39 % CO + 33 % CO_2 + 10 % H_2O + 1 % CH_4, (3) HB 40 % H_2 + 33 % CO + 14 % CO_2 + 11 % H_2O + 2 % CH_4. Three durability tests were conducted, starting by DH for 262 h, followed by CB for 258 h and a test with HB for 231 h.

The degradation behaviour of solid oxide fuel cells under biogas environment has been analysed through health monitoring methods, including EIS, DRT, CNLS fit of the ECM.

The main results can be summarised as follows:

- IV curves and voltage measurements indicated that the CB composition is the one degrading at most, equal to 25.8 mV/kh, followed by DH which shows a degradation rate of 18.6 mV/kh. HB composition had the lowest measured degradation rate of 8.73 mV/kh, while considering this result could be influenced by the cell ageing history. Even if the CB case showed the best performance reaching the highest current density, the larger voltage losses at high load reveal an increase in polarization losses. The enhanced curvature of the IV curve at high current density suggests the contribution of gas diffusion and conversion phenomena, as found also for Ni-GDC ESC.
- DRT results between different gas compositions indicated that CB and HB case demonstrated much lower gas conversion resistance than the DH case, due to the presence of steam. Peaks at medium-high frequency are not affected by different gas compositions.
- Resistance evolution in the CNLS shows that gas conversion resistance (RQ8) is the one varying at most with fuel composition, exhibiting its highest values under dry hydrogen.
- The main degradation is observed with dry hydrogen for RQ6, which represents oxygen electrode reaction and diffusion, likely due to microstructural and chemical evolution at the oxygen electrode. On the other hand, RQ8, RQ5 and RQ4, associated with the gas conversion, oxygen electrode transport and fuel electrode charge-transfer processes respectively, remains relatively unchanged across all conditions. This suggests that no major degradation mechanisms are active under the tested reformate compositions.
- Time constant agrees with the trends in DRT results. The time constants associated with medium-high frequency processes remain remarkably stable over time indicating that mechanisms remain active and unchanged, even if the resistances could change.

Our DRT and CNLS analyses further confirm that the main long-term degradation is associated with oxygen-electrode processes and intermediate-frequency features. In particular, we show that the gas-conversion peak becomes slower and less dominant in biogas, and that the fuel-electrode charge-transfer resistance (RQ4) remains essentially unchanged, indicating limited degradation of the Ni–YSZ interface under the pre-processed biogas compositions.

From a system-design perspective, the results suggest that avoiding cold recirculation (CB) strategies, which generate CO-rich reformates and enhance diffusion-related polarisation losses, is beneficial for long-term durability of anode supported SOFCs. In contrast, hot recirculation (HB) provides a more stable operating window, limiting voltage decay and mitigating gas-transport degradation phenomena.

Importantly, the Ni–YSZ anode maintains its charge-transfer activity throughout all tested fuels, indicating that future durability improvements should primarily focus on cathode-related ageing and gas-management optimisation, rather than on anode poisoning under properly pre-processed biogas feeds.

Acronyms

ASC	Anode supported cell
AU	Air utilisation
CB	Cold biogas recirculation
CNLS	Complex non linear square
DH	Dry hydrogen
DRT	Distribution relaxation times
ECM	Equivalent circuit model
EIS	Electrochemical impedance spectroscopy
ESC	Electrolyte supported cell
FU	Fuel utilisation
GDC	Gadolinium doped ceria
HB	Hot biogas recirculation
KK	Kramers-Kronig
LSC	$(La_{0.6}Sr_{0.4})CoO_{3-\delta}$
LSCF	$(La_xSr_{1-x})Co_yFe_{1-y}O_3$
MFC	Mass flow controller
OCV	Open circuit voltage
SOFC	Solid oxide fuel cell
TPB	Triple phase boundary
WGS	Water gas shift
YSZ	Yttria stabilised zirconia

CRediT authorship contribution statement

Lucia Pera: Writing – original draft, Visualization, Investigation, Formal analysis, Data curation, Conceptualization. **Cédric Frantz:** Writing – review & editing, Visualization, Methodology, Investigation, Formal analysis, Data curation, Conceptualization. **Hangyu Yu:** Writing – review & editing, Visualization, Software, Methodology, Investigation, Formal analysis, Data curation, Conceptualization. **Marta Gandiglio:** Writing – review & editing, Supervision. **Paolo Marocco:** Writing – review & editing, Supervision. **Massimo Santarelli:** Supervision, Funding acquisition. **Jan Van Herle:** Supervision, Funding acquisition.

Declaration of competing interest

The authors declare the following financial interests/personal relationships which may be considered as potential competing interests:

Acknowledgments

The work is supported by National Key Research and Development Program of China (Grant No. 2024YFE0207200) and the Fuel Cells and Hydrogen Joint Undertaking, Belgium under grant agreement No 826234 (Waste2Watts) and No 24.00185 - 101146861 (Niagara), which receive support from the European Union's Horizon 2020 research and innovation programme.

Supplementary materials

Supplementary material associated with this article can be found, in the online version, at doi:10.1016/j.electacta.2026.148838.

Appendix

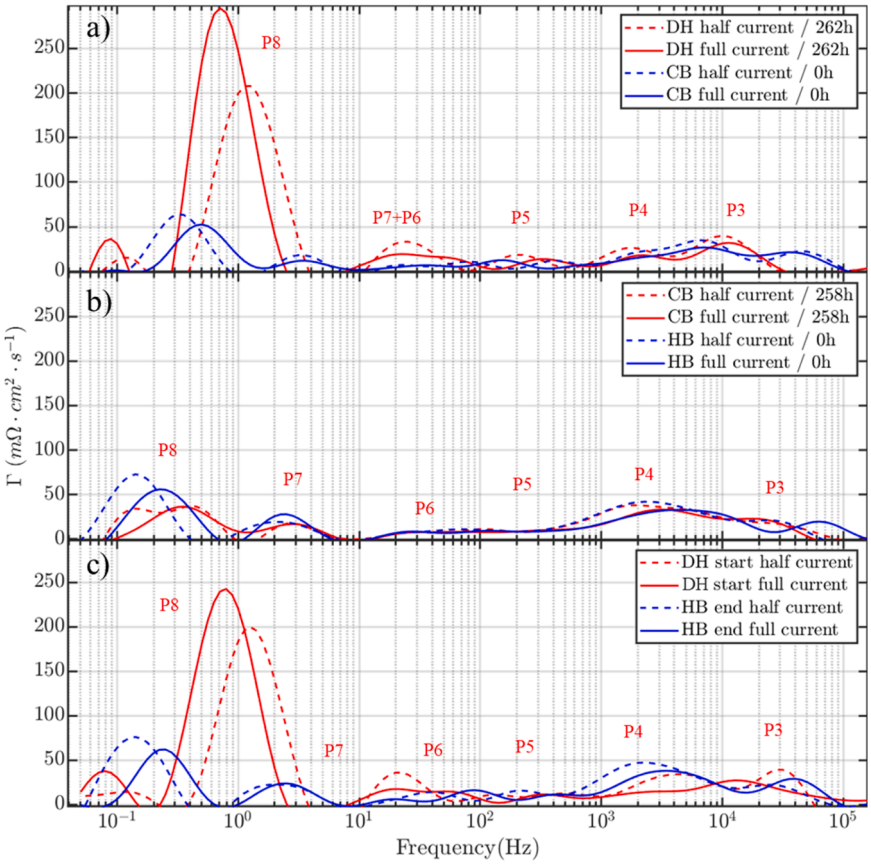

Fig. A.1. DRT results with peaks recognition to compare the degradation rate under different gas composition. Solid line represents the case with full current density and the dashed line represents the case with half current density.

Table A.1 summarises the probability values associated with fitted parameters of an equivalent circuit element, taking as representative the CB case at the beginning of its long-term test at full current density. Low p-values indicate that the parameter is statistically significant and reliably identified by the fitting procedure, whereas higher p-values suggest reduced confidence in the parameter estimate. In general, a parameter is considered statistically significant when its *p*-value is less than 0.05. The comparatively higher *p*-value of τ_6 is consistent with α_6 reaching the imposed lower bound ($\alpha = 0.4$). When α is constrained at its limit (see Table A.1), the RQ element becomes highly dispersed and the impedance response becomes less sensitive to τ. Consequently, τ is less uniquely identifiable even though RQ remains statistically significant.

Overall, the table highlights that the resistive contributions of all elements are reliably fitted, as well as the time-constant estimation and the dispersion factor.

Table A.1
Probability value of the parameters of different elements in CNLS fit, where EIS measurements under the CB environment with full current density in the beginning of the durability test.

Element	Process	Resistance/inductance	Time constant	Dispersion factor
L1	-	$5.24 \cdot 10^{-14}$	-	-
R2	-	$<10^{-16}$	-	-
RQ3	Solid state process	$<10^{-16}$	$<10^{-16}$	$<10^{-16}$
RQ4	Fuel electrode charge transfer	$<10^{-16}$	$8.77 \cdot 10^{-12}$	$<10^{-16}$
RQ5	Oxygen electrode transport and oxygen charge transfer	$<10^{-16}$	0.0736	$<10^{-16}$
RQ6	Oxygen electrode reaction	$<10^{-16}$	0.149	$<10^{-16}$
RQ7	Fuel electrode diffusion	$<10^{-16}$	$<10^{-16}$	$<10^{-16}$
RQ8	Gas conversion	$<10^{-16}$	$<10^{-16}$	$<10^{-16}$

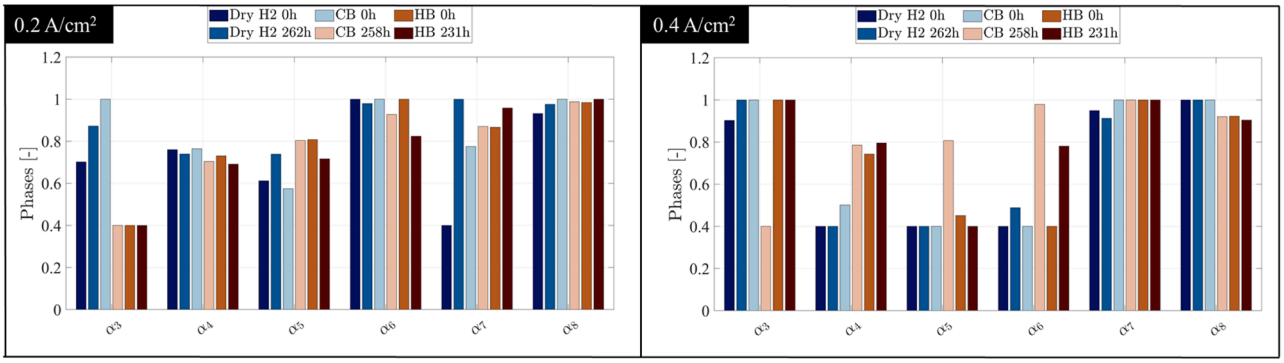

Fig. A.2. Dispersion factor of different elements under different gas environment for case with half current density and full current density.

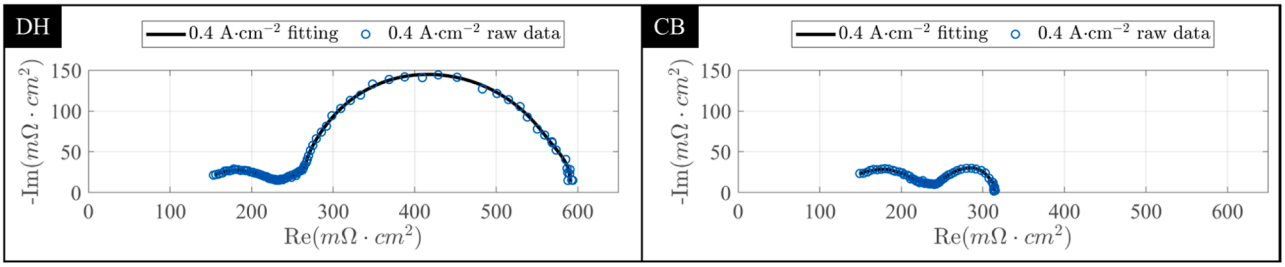

Fig. A.3. EIS fitting and raw data for DH environment and CB environment with full current density in the beginning of the durability test.

Data availability

Data will be made available on request.

References

[1] M. Gandiglio, P. Marocco, A. Nieminen, M. Santarelli, J. Kiviaho, Energy and environmental performance from field operation of commercial-scale SOFC systems, Int. J. Hydrogen Energy 85 (2024) 997–1009, https://doi.org/10.1016/j.ijhydene.2024.08.332.

[2] A.B. Stambouli, E. Traversa, A. Stambouli, Solid oxide fuel cells (SOFCs): a review of an environmentally clean and efficient source of energy. www.elsevier.com/locate/rser, 2002.

[3] S. O'Connor, E. Ehimen, S.C. Pillai, A. Black, D. Tormey, J. Bartlett, Biogas production from small-scale anaerobic digestion plants on European farms, Renew. Sustain. Energy Rev. 139 (2021), https://doi.org/10.1016/j.rser.2020.110580.

[4] M. Gandiglio, A. Lanzini, M. Santarelli, M. Acri, T. Hakala, M. Rautanen, Results from an industrial size biogas-fed SOFC plant (the DEMOSOFC project), Int. J. Hydrogen Energy 45 (2020) 5449–5464, https://doi.org/10.1016/j.ijhydene.2019.08.022.

[5] M.S. Khan, S.B. Lee, R.H. Song, J.W. Lee, T.H. Lim, S.J. Park, Fundamental mechanisms involved in the degradation of nickel–yttria stabilized zirconia (Ni–YSZ) anode during solid oxide fuel cells operation: a review, Ceram. Int. 42 (2016) 35–48, https://doi.org/10.1016/j.ceramint.2015.09.006.

[6] V. Chiodo, A. Galvagno, A. Lanzini, D. Papurello, F. Urbani, M. Santarelli, S. Freni, Biogas reforming process investigation for SOFC application, Energy Convers. Manag. 98 (2015) 252–258, https://doi.org/10.1016/j.enconman.2015.03.113.

[7] H. Yu, C. Frantz, L. Savioz, P. Aubin, D. Fronterotta, C. Geipel, H. Moussaoui, G. Jeanmonod, L. Wang, J. Van herle, Poisoning and recovery behavior of Ni-GDC based electrolyte-supported solid oxide fuel cell exposed to common sulfur compounds under processed biogas environment, J. Power Sources 642 (2025), https://doi.org/10.1016/j.jpowsour.2025.236901.

[8] H. Yu, C. Frantz, L. Savioz, D. Fronterotta, P. Aubin, C. Geipel, G. Jeanmonod, L. Wang, J. Van herle, Parametric study of Ni-GDC based electrolyte-supported cell via electrochemical impedance spectroscopy, SSRN (2025), https://doi.org/10.2139/ssrn.5218765.

[9] X. Wu, Y. Tian, X. Zhou, X. Kong, J. Zhang, W. Zuo, D. Wang, X. Ye, Performance and long-term stability of nickel/yttria-stabilized zirconia anode-supported solid oxide fuel cell in simulated biosyngas, Energy 114 (2016) 1–9, https://doi.org/10.1016/j.energy.2016.07.160.

[10] A. Lanzini, P. Leone, Experimental investigation of direct internal reforming of biogas in solid oxide fuel cells, Int. J. Hydrogen Energy 35 (2010) 2463–2476, https://doi.org/10.1016/j.ijhydene.2009.12.146.

[11] D. Papurello, R. Borchiellini, P. Bareschino, V. Chiodo, S. Freni, A. Lanzini, F. Pepe, G.A. Ortigoza, M. Santarelli, Performance of a solid oxide fuel cell short-stack with biogas feeding, Appl. Energy 125 (2014) 254–263, https://doi.org/10.1016/j.apenergy.2014.03.040.

[12] T. Papadam, G. Goula, I.V. Yentekakis, Long-term operation stability tests of intermediate and high temperature Ni-based anodes' SOFCs directly fueled with simulated biogas mixtures, Int. J. Hydrogen Energy (2012) 16680–16685, https://doi.org/10.1016/j.ijhydene.2012.02.147.

[13] L. Pera, M. Gandiglio, P. Marocco, D. Pumiglia, M. Santarelli, Trace contaminants in biogas: biomass sources, variability and implications for technology applications, J. Environ. Chem. Eng. 12 (2024), https://doi.org/10.1016/j.jece.2024.114478.

[14] L. Yang, Z. Cheng, M. Liu, L. Wilson, New insights into sulfur poisoning behavior of Ni–YSZ anode from long-term operation of anode-supported SOFCs, Energy Environ. Sci. 3 (2010) 1804–1809, https://doi.org/10.1039/c0ee00386g.

[15] J. Ma, Y. Jiang, P.A. Connor, S.R. Gamble, M. Cassidy, C. Jiang, J.T.S. Irvine, Detailed study of sulfur poisoning and recovery of Ni–YSZ-based anodes operating up to 1.8 W cm-2in a biogas fuel, Int. J. Energy Res. 2023 (2023), https://doi.org/10.1155/2023/2339117.

[16] A. Hauch, A. Hagen, J. Hjelm, T. Ramos, Sulfur poisoning of Ni/stabilized-zirconia anodes – effect on long-term durability, ECS Trans. 57 (2013) 615–625, https://doi.org/10.1149/05701.0615ecst.

[17] A. Weber, S. Dierickx, A. Kromp, E. Ivers-Tiffée, Sulfur poisoning of anode-supported SOFCs under reformate operation, Fuel Cells 13 (2013) 487–493, https://doi.org/10.1002/fuce.201200180.

[18] L. Pera, M. Gandiglio, P. Marocco, D. Pumiglia, L. Della Seta, M. Santarelli, Impact of trace contaminants on SOFC operated with bio-syngas: sulphur and siloxane-induced degradation, J. Power Sources 665 (2026) 238967, https://doi.org/10.1016/j.jpowsour.2025.238967.

[19] D. Papurello, A. Lanzini, D. Drago, P. Leone, M. Santarelli, Limiting factors for planar solid oxide fuel cells under different trace compound concentrations, Energy 95 (2016) 67–78, https://doi.org/10.1016/j.energy.2015.11.070.

[20] H. Moussaoui, G. Hammerschmid, J. Van herle, V. Subotić, Fast online diagnosis for solid oxide fuel cells: optimisation of total harmonic distortion tool for real-system application and reactants starvation identification, J. Power Sources 556 (2023), https://doi.org/10.1016/j.jpowsour.2022.232352.

[21] S. Ma, G. Loreti, L. Wang, F. Maréchal, J. Van herle, C. Dong, Comparison and optimization of different fuel processing options for biogas-fed solid-oxide fuel cell plants, Int. J. Hydrogen Energy 47 (2022) 551–564, https://doi.org/10.1016/j.ijhydene.2021.10.025.

[22] H. Madi, Investigations into the effects of biofuel contaminants on solid oxide fuel cells, EPFL (2016), https://doi.org/10.5075/epfl-thesis-7161 (accessed December 9, 2025).

[23] A. Calbry-Muzyka, H. Madi, F. Rüsch-Pfund, M. Gandiglio, S. Biollaz, Biogas composition from agricultural sources and organic fraction of municipal solid waste, Renew. Energy 181 (2022) 1000–1007, https://doi.org/10.1016/j.renene.2021.09.100.

[24] S. Ma, G. Loreti, L. Wang, A. Luigi Facci, S. Ubertini, C. Dong, F. Maréchal, J. Van Herle, Comparison of integrated fuel processing options for biogas-fed solid-oxide

fuel cell plants, in: E3S Web of Conferences, EDP Sciences, 2021, https://doi.org/10.1051/e3sconf/202123804002.
[25] CORDIS European Commision, Unlocking unused bio-WASTE resources with loW cost cleAning and thermal inTegration with solid oxide fuel cells, (n.d.). https://cordis.europa.eu/project/id/826234/results (accessed March 17, 2026).
[26] H. Yu, C. Frantz, L. Savioz, D. Fronterotta, P. Aubin, C. Geipel, H. Moussaoui, G. Jeanmonod, L. Wang, J. Van herle, Characterization of Ni-GDC based electrolyte-supported cell under processed biogas composition: electrochemical performance, degradation and recovery, Electrochim. Acta 526 (2025), https://doi.org/10.1016/j.electacta.2025.146163.
[27] P. Caliandro, A. Nakajo, S. Diethelm, J. Van herle, Model-assisted identification of solid oxide cell elementary processes by electrochemical impedance spectroscopy measurements, J. Power Sources 436 (2019), https://doi.org/10.1016/j.jpowsour.2019.226838.
[28] A. Hauch, A. Hagen, J. Hjelm, T. Ramos, Sulfur poisoning of SOFC anodes: effect of overpotential on long-term degradation, J. Electrochem. Soc. 161 (2014) F734–F743, https://doi.org/10.1149/2.080406jes.
[29] D. Montinaro, A.R. Contino, A. Dellai, M. Rolland, Determination of the impedance contributions in anode supported solid oxide fuel cells with (La,Sr)(Co,Fe)O3-δ cathode, Int. J. Hydrogen Energy 39 (2014) 21638–21646, https://doi.org/10.1016/j.ijhydene.2014.09.081.
[30] G. Brus, H. Iwai, A. Sciazko, M. Saito, H. Yoshida, J.S. Szmyd, Local evolution of anode microstructure morphology in a solid oxide fuel cell after long-term stack operation, J. Power Sources 288 (2015) 199–205, https://doi.org/10.1016/j.jpowsour.2015.04.092.
[31] S. Vafaeenezhad, A.R. Hanifi, M.A. Laguna-Bercero, T.H. Etsell, P. Sarkar, Microstructure and long-term stability of Ni–YSZ anode supported fuel cells: a review, Mater. Fut. 1 (2022), https://doi.org/10.1088/2752-5724/ac88e7.
[32] Z. Lyu, H. Li, M. Han, Z. Sun, K. Sun, Performance degradation analysis of solid oxide fuel cells using dynamic electrochemical impedance spectroscopy, J. Power Sources 538 (2022), https://doi.org/10.1016/j.jpowsour.2022.231569.